

*Citation for published version:*

Chen, Q, Zang, J, Birchall, J, Ning, DZ, Zhao, X & Gao, J 2020, 'On the hydrodynamic performance of a vertical pile-restrained WEC-type floating breakwater', *Renewable Energy*, vol. 146, pp. 414-425.  
<https://doi.org/10.1016/j.renene.2019.06.149>

*DOI:*

[10.1016/j.renene.2019.06.149](https://doi.org/10.1016/j.renene.2019.06.149)

*Publication date:*

2020

*Document Version*

Peer reviewed version

[Link to publication](#)

*Publisher Rights*

CC BY-NC-ND

## University of Bath

**General rights**

Copyright and moral rights for the publications made accessible in the public portal are retained by the authors and/or other copyright owners and it is a condition of accessing publications that users recognise and abide by the legal requirements associated with these rights.

**Take down policy**

If you believe that this document breaches copyright please contact us providing details, and we will remove access to the work immediately and investigate your claim.

# On the hydrodynamic performance of a vertical pile-restrained WEC-type floating breakwater

Qiang Chen<sup>a,b</sup>, Jun Zang<sup>a,b,\*</sup>, Jonathan Birchall<sup>a</sup>, Dezhi Ning<sup>b</sup>, Xuanlie Zhao<sup>b</sup>,  
Junliang Gao<sup>c</sup>

<sup>a</sup>*Research Unit for Water, Environment and Infrastructure Resilience (WEIR), Department of  
Architecture and Civil Engineering, University of Bath, BA2 7AY, U.K.*

<sup>b</sup>*State Key Laboratory of Coastal and Offshore Engineering, Dalian University of Technology, Dalian,  
116024, China*

<sup>c</sup>*School of Naval Architecture and Ocean Engineering, Jiangsu University of Science and Technology,  
Zhenjiang, 212003, China*

---

## Abstract

This paper presents a numerical study on the hydrodynamic performance of a vertical pile-restrained wave energy converter type floating breakwater. The aims are to further understand the characteristics of such integrated system in terms of both wave energy extraction and wave attenuation, and to provide guidance for optimising the shape of the floating breakwater for more energy absorption and less wave transmission at the same time. The numerical model solves the incompressible Navier-Stokes equations for free-surface flows using the particle-in-cell method and incorporates a Cartesian cut cell based strong coupling algorithm for fluid-structure interaction. The numerical model is first validated against an existing experiment, consisting of a rectangular box as the floating breakwater and a power take-off system installed above the breakwater, for the computation of the capture width ratio and wave transmission coefficients. Following that, an optimisation study based on the numerical model is conducted focusing on modifying the shape of the floating breakwater used in the experiment. The results indicate that by changing only the seaward side straight corner of the rectangular box to a small curve corner, the integrated system achieves significantly more wave energy extraction at the cost of only a slight increase in wave transmission.

**Keywords:** Wave energy converters, Floating breakwater, Particle-In-Cell method, CFD

---

\*Corresponding author.

Email address: [j.zang@bath.ac.uk](mailto:j.zang@bath.ac.uk) (Jun Zang)

## 1. Introduction

For coastal areas with high tidal range and/or large water depth, floating breakwaters are frequently used as wave-attenuation structures, due to a number of advantages such as low environmental impact and flexibility [1]. Floating breakwaters with rectangular cross-sections, typically termed as box-type floating breakwaters [1], are widely adopted as they are simple, durable and cost-effective. Meanwhile, in the wave energy field, wave energy converters (WECs) of various types such as oscillating buoys, floating ducks and enclosed chambers have been investigated; nevertheless, cost reduction still remains a big challenge and requires advances [2]. It is found that the box-type floating breakwaters are similar to the oscillating buoy WECs in many aspects such as working conditions, structural characteristics and applied functions. Thus, the idea of integrating WECs into floating breakwaters provides a promising way to realize cost-sharing in wave energy technology [3]. The major concerns with respect to such integrated system include both the performance of wave attenuation and efficiency of power output. A number of pioneering studies show that it is possible to simultaneously realize the function of wave energy utilisation and desired-level wave attenuation for such integrated systems [4, 5, 6].

Ning et al. [6] experimentally studied the system of a vertical pile-restrained floating breakwater that is working under the principle of an oscillating buoy WEC. The integrated system comprises a rectangular box-type floating breakwater as base structure, with a power take-off (PTO) system installed above the breakwater without changing the geometry of the breakwater. Fig. 1 shows a schematic demonstrating the working principle of the integrated system. That is, the kinetic energy of the heave motion of the floating breakwater is captured by the above PTO system through mechanic transmission. The PTO damping force in turn affects the heave motion of the floating breakwater and hence the wave transmission coefficient. Their experimental results show that with the proper adjustment of PTO damping force, a range can be observed for which the capture width ratio (CWR, the ratio of captured energy and incident wave energy) of the system can achieve approximately 24%, with the transmission coefficient being lower than 0.50.

In this paper, the experimental setup used in Ning et al. [6] has been numerically studied using a Particle-In-Cell (PIC) method based model. The aims are to first validate the numerical model for simulating the performance of such WEC-type floating breakwater, and then apply the numerical model to a further optimisation study of the integrated system. It is understood that the rectangular box-type floating breakwater can lead to strong eddy making damping due to the straight corners and therefore small heave motion and hence

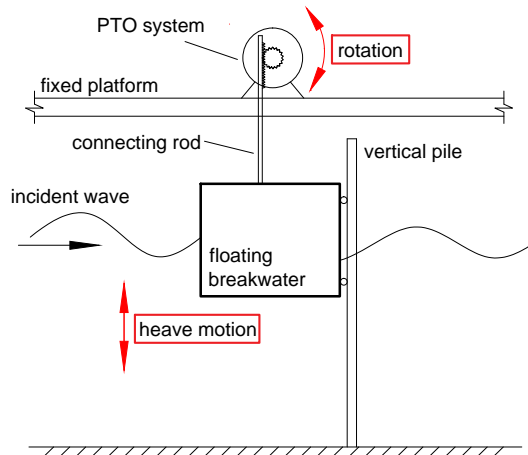


Fig. 1: Sketch (side view) of the integrated system.

47 low efficiency of wave energy transfer. On the other hand, because in the current system  
 48 the floating breakwater has only heave motion, the straight corners can result in large  
 49 wave reflection and therefore desired low wave transmission. Thus, the shape of the floating  
 50 breakwater could be one of the predominant factors to the success of such integrated system.  
 51 In the present work, the focus is on modifying the straight corners of the rectangular box-  
 52 type floating breakwater to curve corners in order to reduce the eddy making damping  
 53 due to wave-structure interaction. We show that by using the curve corner with a proper  
 54 size and position, the motion of the floating breakwater can be increased significantly (and  
 55 hence larger CWR coefficient), while the wave transmission coefficient is still kept within an  
 56 acceptable level.

57 The numerical model used in the present study employs the hybrid Eulerian-Lagrangian  
 58 PIC method to solve the incompressible Navier-Stokes equations (NSE) for single-phase free-  
 59 surface flows, and incorporates a Cartesian cut cell based two-way strong coupling algorithm  
 60 for fluid-structure interaction. The model is capable of simulating complex water-wave sce-  
 61 narios involving large free-surface deformations and the interaction of such flow with surface-  
 62 piercing floating bodies of arbitrary configuration and degree of freedom. Moreover, as a  
 63 Navier-Stokes solver, the viscous effects such as the eddy making damping are automatically  
 64 accounted for. The PIC method dates back to 1950s [7, 8], and was devised with an aim to  
 65 tackle the disadvantages of traditional Eulerian and Lagrangian methods [9]. The idea was  
 66 to combine the uses of an Eulerian grid and a set of Lagrangian particles. In particular, the  
 67 particles are used to solve any transport terms and track the fluid configuration such that  
 68 sharp features of material interfaces can be captured, while the Eulerian grid is employed to

69 solve the rest non-advection terms with computational robustness and efficiency. The early  
70 versions of the PIC method was successful but had many restrictions and difficulties, such as  
71 the large amount of particles required (hence large computing memory storage), relatively  
72 large numerical dissipation and low order of accuracy. Further developments can be found  
73 in, for example, Brackbill and Ruppel [10] and Brackbill et al. [11], which significantly re-  
74 duce the numerical dissipation of PIC method. Recently, variations of the PIC method have  
75 achieved high-order accuracy (see Edwards and Bridson [12], Maljaars et al. [13] and Wang  
76 and Kelly [14]).

77 The PIC method has not attracted sufficient attention from the coastal and offshore  
78 engineering community until very recently. Kelly [15] initially proposed a PIC model for  
79 simulating solitary wave propagating onto a slop beach in two spatial dimensions (2D). Then,  
80 Kelly et al. [16] applied a PIC model augmented with a distributed Lagrange multiplier  
81 (DLM) method to handle problems that involve full two-way fluid-solid coupling. Later,  
82 Chen et al. [17] proposed a Cartesian cut cell based two-way strong fluid-solid coupling  
83 algorithm within their two-dimensional PIC model, which was further extended by Chen  
84 et al. [18] to three spatial dimensions with domain decomposition based message passing  
85 interface (MPI) parallelisation. These studies have shown that the PIC method has great  
86 potential to become a high-quality CFD tool for use in coastal and offshore engineering  
87 applications. In fact, the PIC model used in this study is developed based on that proposed  
88 in Chen et al. [17]. We show that this PIC model can satisfactorily capture the key physical  
89 processes occurring in the scenario of wave interaction with a WEC-type floating breakwater.

90 The paper is organised as follows: [Section 2](#) gives an overview of the current PIC model  
91 including the governing equations and major numerical implementations. Next, in [Section 3](#)  
92 the numerical model is first validated for simulating wave interaction with the integrated  
93 system of WEC-type floating breakwater using the experiment proposed in Ning et al. [6],  
94 and then an optimisation study based on the numerical model is conducted focusing on  
95 modifying the shape of the floating breakwater in the experiment. Finally, in [Section 4](#)  
96 conclusions are drawn.

## 97 **2. Numerical Model**

### 98 *2.1. Governing equations*

99 The current PIC model solves the incompressible Newtonian Navier-Stokes equations  
100 for single-phase flow, and incorporates a Cartesian cut cell based two-way strong fluid-solid

101 coupling algorithm for fluid-structure interaction. The governing equations are:

$$\nabla \cdot \mathbf{u} = 0, \quad (1)$$

102

$$\frac{\partial \mathbf{u}}{\partial t} + (\mathbf{u} \cdot \nabla) \mathbf{u} = \mathbf{f} - \frac{1}{\rho} \nabla p + \nu \nabla^2 \mathbf{u}, \quad (2)$$

103 with the following boundary conditions applied on the free surface and the freely moving  
104 structure surface:

$$p = 0 \quad \text{on } \zeta(\mathbf{x}, t), \quad (3)$$

105 where  $\zeta(\mathbf{x}, t)$  represents the free-surface position and

$$\mathbf{u} = \mathbf{U}_b \quad \text{and} \quad \mathbf{n} \cdot (\Delta t \rho^{-1} \nabla p) = \mathbf{n} \cdot (\tilde{\mathbf{U}}_b - \mathbf{U}_b^{n+1}) \quad \text{on } \partial\Omega_S(\mathbf{x}, t), \quad (4)$$

106 where  $\partial\Omega_S$  represents the structure surface. In 2D,  $\mathbf{u} = [u, w]^T$  is the velocity field,  $p$  is  
107 pressure,  $t$  is time,  $\mathbf{f} = [0.0, -9.81 \text{ m/s}^2]^T$  represents the body force due to gravity, and  $\nu$   
108 and  $\rho$  are the kinematic viscosity and density of the fluid respectively. In Eq. 4,  $\tilde{\mathbf{U}}_b$  denotes  
109 a tentative velocity on the structure surface between  $\mathbf{U}_b^n$  and  $\mathbf{U}_b^{n+1}$ , which represent the  
110 velocities on the structure surface at time steps  $n$  and  $n + 1$  respectively, and  $\mathbf{n}$  is the unit  
111 outward normal vector of the structure surface. For full details of the equations solved in  
112 the current PIC model, the reader is referred to Chen et al. [17] and Chen [19].

## 113 2.2. Numerical solution procedure

114 The current PIC model employs the full particle PIC methodology following Brackbill  
115 and Ruppel [10]. The whole computational domain is discretised by a staggered Eulerian  
116 grid, and the fluid area is accommodated by a set of Lagrangian particles. Fig. 2 shows  
117 a schematic of the computational setup. To reduce numerical dissipation, all the fluid  
118 properties such as the mass and momentum are carried by the particles. At the beginning of  
119 each computational cycle, the velocity field carried by the particles is mapped onto the grid  
120 using a kernel interpolation that conserves the mass and momentum (see Chen et al. [18]).  
121 The free-surface position is also reconstructed on the grid based on the particle location.  
122 Then, the governing equations ignoring the advection term are solved on the grid using a  
123 pressure projection method proposed in Chorin [20]. During this stage, a pressure Poisson  
124 equation (PPE) is constructed and solved in a finite volume sense involving all the boundary  
125 conditions. Particularly, the Cartesian cut cell method based two-way strong fluid-solid  
126 coupling algorithm is employed to resolve the boundary conditions applied on the structure

127 surface. Once this is done, a divergence-free velocity field and an acceleration field (i.e.  
 128 velocity change) are obtained on the grid, which are then used to update the velocity field  
 129 carried by the particles. Finally, the particles are moved to solve the remaining advection  
 130 term and update the fluid configuration. Fig. 3 shows a general algorithm of the PIC model,  
 131 where the changes of the main variables following each step are also given. As the Lagrangian  
 132 particles are used to track the free surface, sharp features as well as large deformations of the  
 133 fluid interface can be well captured; meanwhile, the employment of an Eulerian grid makes  
 134 the model both efficient and robust when handling complex free-surface flow problems.  
 135 Equally importantly, the aforementioned fluid-solid interaction scheme enables the model to  
 136 simulate freely moving structures of arbitrary shape and degree of freedom. For full detail  
 137 of the current PIC model, the interested reader is referred to Chen et al. [17] and Chen [19].

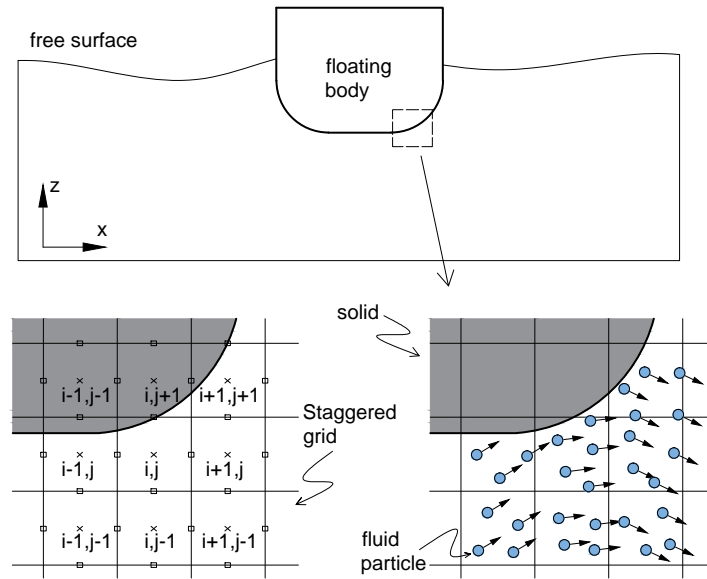


Fig. 2: Sketch of the computational domain, the staggered grid and fluid particles.

138

### 139 3. Model validation and optimisation study

140 In this section, the experiment of a vertical pile-restrained WEC-type floating breakwater  
 141 presented in Ning et al. [6] is first used to validate the present PIC model. After that,  
 142 an optimisation study based on the numerical model is conducted to further exploit the  
 143 potential of the integrated system in the experiment. This is via changing the shape the

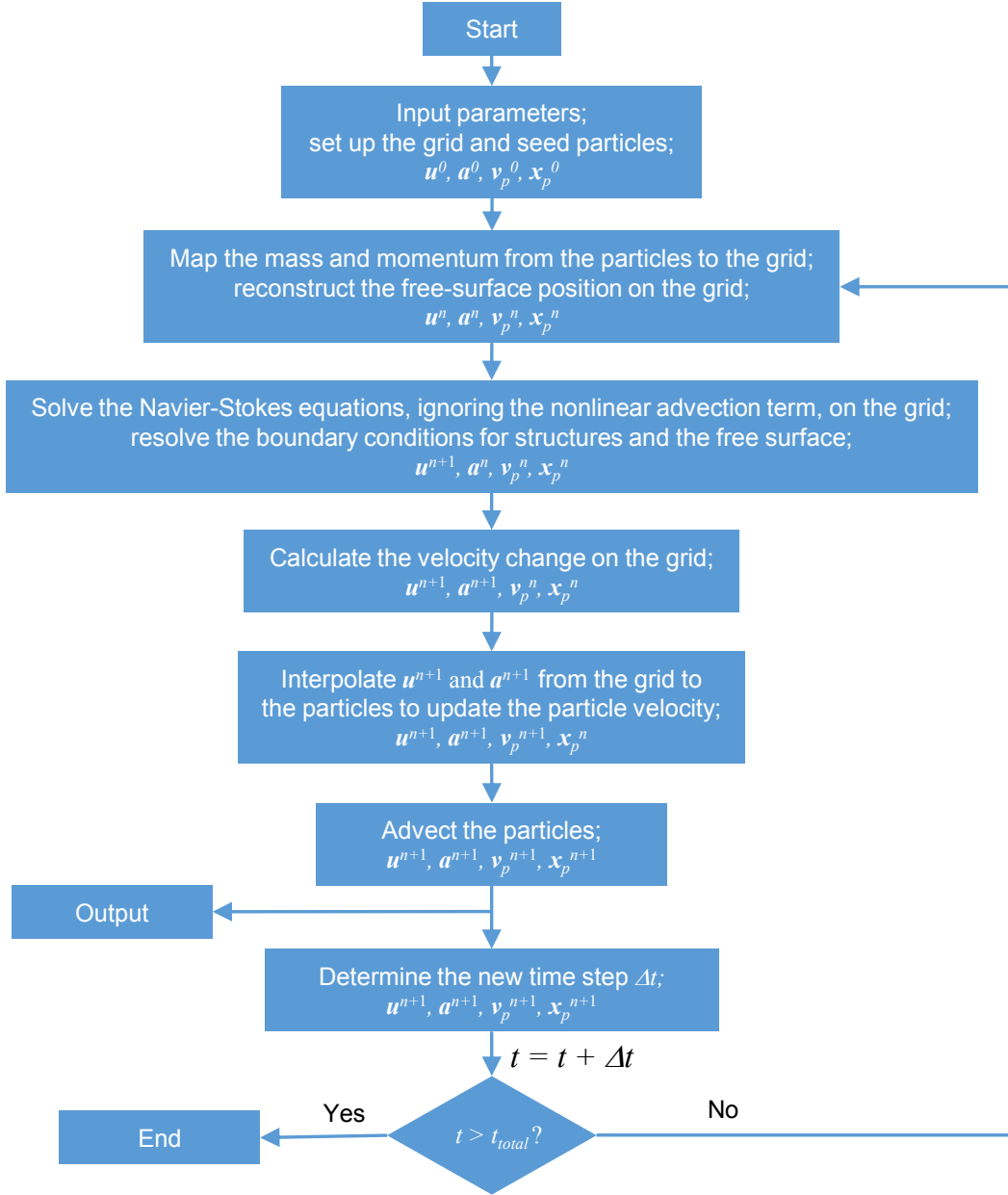


Fig. 3: A schematic showing the general algorithm of the PIC model.  $\mathbf{u}$  and  $\mathbf{a}$  are the velocity and the velocity change on the grid,  $\mathbf{v}_p$  and  $\mathbf{x}_p$  are the particle velocity and particle position, and  $n$  denotes the time level.  $\mathbf{a}^{n+1} = \mathbf{u}^{n+1} - \mathbf{u}^n$ .

144 floating breakwater so as to obtain more wave energy extraction but less wave transmission  
 145 at the same time.



### 146 3.1. Experimental setup

147 The experiment of Ning et al. [6] was conducted in a wave flume at the State Key  
148 Laboratory of Coastal and Offshore Engineering, Dalian University of Technology, China.  
149 A piston-type unidirectional wavemaker is installed at one end of the flume, and a wave-  
150 absorbing beach is located at the other end to reduce the wave reflection. Fig. 4 shows a  
151 sketch depicting the setup of the physical model. The integrated system consisted of a ver-  
152 tical pile-restrained floating breakwater and a PTO system installed above the breakwater  
153 without changing the structure of the breakwater. The breakwater was restricted to heave  
154 motion only under wave action. Pulleys were used to connect the floating breakwater and  
155 the vertical pile. The friction coefficient between the pulley and the slide rail was 0.035  
156 (determined by a friction coefficient measurement test). Note that the dimensions of the  
157 cross-section of the vertical pile were sufficiently small so that their influence on the wave  
158 field can be neglected. The heave motion of the breakwater was converted to the rotary  
159 motion of the shaft in the PTO system through the meshing engagement of a toothed rack  
160 on the connecting rod and a gear fixed at one end of the shaft (see Fig. 4). A current  
161 controller-magnetic powder brake system, which can produce approximate Coulomb damp-  
162 ing force [6], and a torque-power sensor, which was used to measure the torque on the shaft,  
163 were connected to the other end of the shaft to simulate the power generation system (see  
164 Fig. 4). The PTO damping force was set by adjusting the input excitation current by the  
165 current controller. Four wave gauges were used to measure the free surface elevations as  
166 the experiment progressed; their locations are indicated in Fig. 4. The breakwater was a  
167 rectangular box measuring 0.8 m wide ( $B$ ), 0.6 m high and 0.78 m long ( $D$ ) in the transverse  
168 direction, with the gap between the breakwater and the flume wall being 0.01 m. The water  
169 depth  $h$  was fixed at 1.0 m, while the draft of the breakwater changed according to the test  
170 cases under consideration. Only regular waves were tested in the experiment and the test  
171 conditions are given in the following section. For more details about the experimental setup,  
172 the reader is referred to Ning et al. [6].

### 173 3.2. Numerical setup

174 In the present work, a 2D numerical wave tank (NWT) is established following Chen  
175 et al. [21]. Waves are generated in the  $x$ -direction using a piston-type wave paddle, which  
176 is installed at one end of the NWT (in the  $x$ -direction). At the other end, a relaxation  
177 zone is employed for wave absorption. The velocities of any particles that have entered the  
178 relaxation zone are gradually damped out. We note that in order to save on CPU cost,  
179 the length of the NWT was modified for different wave conditions. For example, a short

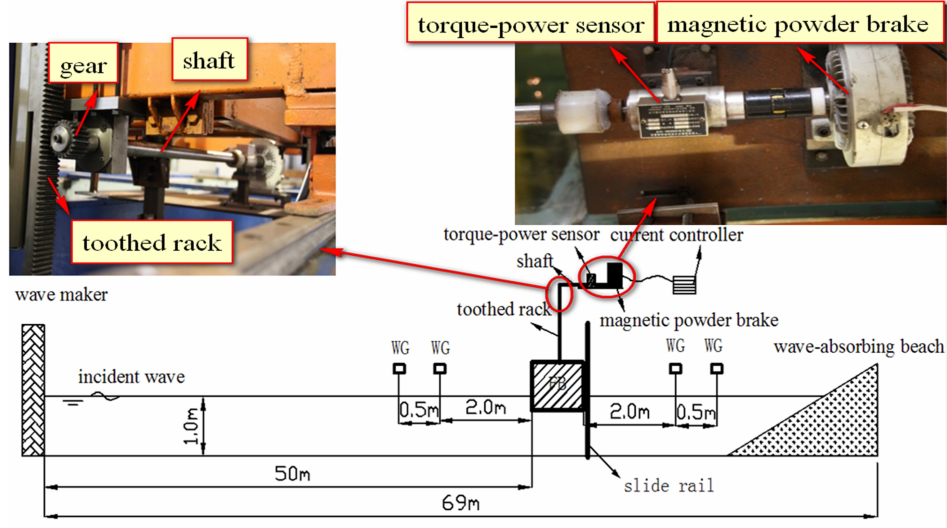


Fig. 4: A sketch of the experimental setup. WG: wave gauge. This figure is reprinted from Ning et al. [6], Copyright (2016), with permission from Elsevier.

180 NWT was used when the incident regular wave has a short wavelength. However, the floating  
 181 breakwater was always placed at a position approximately 6 wavelengths away from the wave  
 182 paddle to ensure that the motion of the floating breakwater is fully developed to a steady  
 183 state before being contaminated by the re-reflected waves from the wavemaker. Having  
 184 a shorter computational domain is also beneficial in terms of minimising any unwanted  
 185 numerical diffusion that may be present. The length of the relaxation zone was kept at  
 186 least 2 wavelengths long for each test condition in order to achieve the most cost-effective  
 187 performance of wave absorption in the current PIC model [19].

188 The grid sizes were chosen as  $\Delta x = \Delta z = 0.02$  m according to a grid convergence study,  
 189 which is given in Section 3.4.1. The time step was controlled by the Courant number that  
 190 was set to 0.5 for all the test cases.

191 In the numerical modelling, the PTO damping force  $F_{PTO}$  directly applied on the floating  
 192 breakwater was in a standard Coulomb form as demonstrated in Fig. 5. The magnitude  $F$   
 193 of  $F_{PTO}$  was controlled by the input excitation current  $I$ , and their relations are given in  
 194 Section 3.3. Note that the PTO damping force was always in the opposite direction of the  
 195 heave motion of the floating breakwater. Another external force due to the friction between  
 196 the pulleys and the slide rail was applied in the same manner, except that the magnitude of  
 197 the friction force was determined by  $\mu F_h(t)$ , where  $\mu$  is the friction coefficient and  $F_h(t)$  is  
 198 the horizontal wave force on the breakwater at time  $t$ .

199 In the physical experiment, the captured energy by the PTO system was analysed using

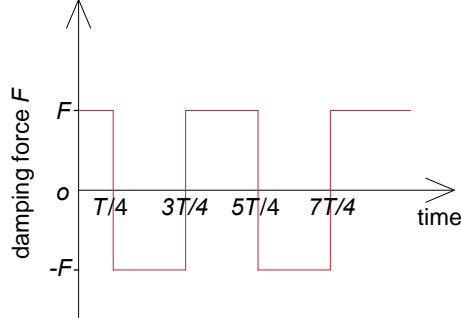


Fig. 5: A sketch showing the standard Coulomb damping force applied on the floating breakwater in the numerical simulation.  $F$  is the magnitude of the damping force and  $T$  is the wave period.

200 the power curve measured by the torque-power sensor that was installed between the shaft  
 201 and the magnetic powder brake. In the numerical model, this is calculated equivalently  
 202 using the PTO damping force:

$$P_c = 4F\delta/T, \quad (5)$$

203 where  $P_c$  is the captured wave power;  $F$  is the magnitude of the PTO damping force;  $\delta$  is  
 204 the amplitude of the heave motion of the floating breakwater and  $T$  is the wave period. The  
 205 incident wave power is calculated by:

$$P_i = \frac{1}{16} \frac{\rho g H_i^2 \omega D}{k} \left( 1 + \frac{2hk}{\sinh 2hk} \right), \quad (6)$$

206 where  $h$  is the water depth;  $k$  is the wave number;  $H_i$  is the incident wave height;  $\omega$  is the  
 207 wave frequency and  $D$  is the transverse length of the floating breakwater. Consequently, the  
 208 CWR coefficient  $\eta = P_c/P_i$ .

209 The wave transmission coefficient  $K_t$  in the numerical model is calculated as  $H_t/H_i$ ,  
 210 where  $H_i$  is the incident wave height and  $H_t$  is the transmission wave height. The trans-  
 211 mission wave height is calculated using the steady-state free-surface elevation extracted at  
 212 the location of the first wave gauge behind the floating breakwater (see Fig. 4). It is noted  
 213 that for all of the test cases, the transmission wave heights are all calculated using this  
 214 wave gauge, which ensures consistency for obtaining the characteristic trend of the wave  
 215 transmission coefficient.

### 216 3.3. Test conditions

217 Regular waves were used in the experiment. The test conditions of the selected test cases  
 218 for validating the numerical model and the optimisation study are all given in Table 1, where

Table 1: Parameters of the test cases.

Test case	$d$ (m)	$T$ (s)	$B/L$	floating breakwater	Test type
1	0.20	1.16, 1.37, 1.58, 1.79, 2.00, 2.42	0.38, 0.28, 0.22, 0.18, 0.15, 0.12	Box	Validation
2	0.25	1.37, 1.58	0.28, 0.22	Box	Validation
3	0.25, 0.27, 0.30	1.37	0.28	Box	Validation
4	0.25	1.37, 1.58	0.28, 0.22	Models 1, 2, 3	Optimisation
5	0.25, 0.27, 0.30	1.37	0.28	Models 1, 2, 3	Optimisation
6	0.25	1.37, 1.58	0.28, 0.22	Models 4, 5	Optimisation

219  $d$  is the draft of the floating breakwater,  $T$  is the wave period and  $L$  is the wavelength. Test  
 220 cases 1-3 are validation cases, where experimental data are available for comparison and the  
 221 floating breakwater is the rectangular box. Test cases 4 and 5 are optimisation study cases,  
 222 where models 1-5 represent the modified breakwaters, whose shapes are sketched in Fig. 6.  
 223 As shown in Fig. 6, models 1-3 have curve corners for both the seaward and the leeward  
 224 sides, with their radii  $R$  ranging from 0.1 m to 0.4 m (full curve). Furthermore, models 4  
 225 and 5 are asymmetric and have one curve corner ( $R = 0.1$  m) and one straight corner (as  
 226 the rectangular box). In particular, while model 4 has a seaward side curve corner, model 5  
 227 has a leeward side curve corner.

228 For the validation cases, test case 1 considers one draft and six different incident wave  
 229 periods, and the excitation current was kept constant to  $I = 0.0$ , i.e. no PTO damping  
 230 force. With the inclusion of the PTO system, test case 2 looks into the effect of incident  
 231 wave period on the hydrodynamic performance of the integrated system, and test case 3  
 232 focuses on the effect of the draft of the floating breakwater. Note that as the draft of the  
 233 floating breakwater increases, the mass of the breakwater increases. For the optimisation  
 234 study, the test conditions are all kept the same as those in the validation cases according to  
 235 the test cases under consideration, with only different breakwaters as given in Fig. 6.

236 For each test case, the magnitudes of the PTO damping forces corresponding to the  
 237 input excitation currents are digitised from Ning et al. [6] and given in Table 2. For all the  
 238 test cases, the incident wave height  $H_i$  was fixed at 0.2 m.

### 239 3.4. Validation results and discussions

240 In this section, the numerical results from the present PIC model are compared with  
 241 those from the experiment of Ning et al. [6]. Prior to that, a grid convergence study based  
 242 on a free decay test is conducted to determine the grid size, and the capability of the present  
 243 numerical model on predicting wave forces are also tested. For the latter, as no experimental  
 244 data are available from Ning et al. [6], the experiment presented in Rodriguez and Spinneken

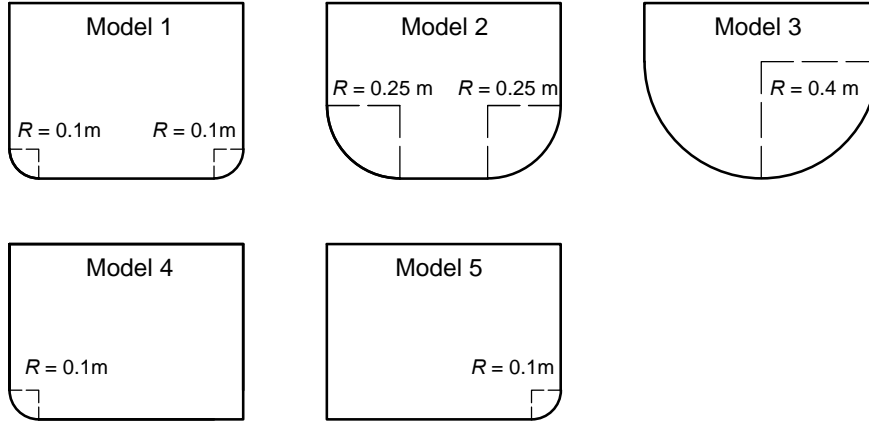


Fig. 6: Sketch showing the shapes of the designed breakwaters for the optimisation study.  $R$  is the radius of the curve corner.

Table 2: Magnitude of the PTO damping force for different test cases.

Test case	$d$ (m)	$T$ (s)	Excitation current $I$ (A)	$F$ (N)
1	0.20	the same as Table 1	0.00	0.00
2	0.25	1.37	0.06, 0.12, 0.18, 0.24, 0.30	13.85, 44.68, 80.00, 115.67, 130.91
	0.25	1.58	0.06, 0.12, 0.18, 0.24, 0.30	17.96, 43.00, 84.60, 121.21, 142.96
3	0.25	1.37	0.06, 0.12, 0.18, 0.24, 0.30	the same as Test case 2
	0.27	1.37	0.06, 0.12, 0.18, 0.24, 0.30	19.75, 52.66, 77.22, 107.34, 134.68
	0.30	1.37	0.06, 0.12, 0.18, 0.24, 0.30	15.44, 47.34, 87.59, 118.48, 130.13
4	0.25	1.37, 1.58	0.06, 0.12, 0.18, 0.24, 0.30	the same as Test case 2
5	0.25,0.27,0.30	1.37	0.06, 0.12, 0.18, 0.24, 0.30	the same as Test case 3
6	0.25	1.37,1.58	0.06, 0.12, 0.18, 0.24, 0.30	the same as Test case 2

245 [22] are adopted, where both the wave and structure characteristics are similar to those used  
 246 in Ning et al. [6] and experimental data regarding wave forces are available.

### 247 3.4.1. Grid convergence study

248 Grid convergence studies were carried out to determine the grid size for the current  
 249 numerical simulations. These were based on the free decay tests of the heave motion of the  
 250 floating breakwater for the rectangular box and Model 2 (see Fig. 6). Initially, the floating  
 251 breakwater had a draft of 0.25 m and no PTO damping force was considered. The floating  
 252 breakwater was then lifted up by approximately 0.24 m and released, resulting in a free  
 253 motion of vertical oscillation. Three different grid sizes were used for the tests; they were  
 254  $\Delta x = \Delta z = B/20$  (the coarse grid),  $B/40$  (the moderate grid) and  $B/80$  (the fine grid),

255 where  $B = 0.8$  m is the width of the floating breakwater. Fig. 7 shows the results for the  
 256 three grid sizes. In particular, for the rectangular box case, the experimental data are also  
 257 available for comparison. In terms of the convergence study, it may be seen from Fig. 7 that  
 258 for both floating breakwater shapes the heave motion produced by the moderate grid tends  
 259 to have a smaller discrepancy than that by the coarse grid, when compared with the result by  
 260 the fine grid. Using the result of the fine grid as reference and taking 80 points equally across  
 261 the time range from 0.056 s to 4.006 s, the root mean square errors (RMSE) of the results  
 262 by the moderate and the coarse grid are 0.00295 and 0.00505 for the rectangular box case  
 263 and 0.00139 and 0.00289 for Model 2 case (see Fig. 6), respectively. Both data pairs show  
 264 that the results are converging. Note that because the present PIC model uses a double-grid  
 265 system (i.e. grid and particles), the memory storage requirement is very demanding for the  
 266 fine grid case. Considering that the results by the moderate grid are very close to those  
 267 of the fine grid, the moderate grid ( $\Delta x = \Delta z = B/40$ ) is finally chosen for the numerical  
 268 simulations.

269 Regarding the comparison between the numerical and experimental results for the rect-  
 270 angular box case, it can be seen that the experimental data show a longer natural period  
 271 and larger damping of the integrated system. This is due to the fact that the effect of the  
 272 rotary motion of the shaft in the PTO system (see Fig. 4) is neglected in the numerical  
 273 simulations, which is because of a lack of dimension and weight information for the shaft  
 274 from the experiment. The shaft in fact adds to the overall mass of the integrated system  
 275 and hence increases its natural period. Moreover, the frictions in the experiment due to the  
 276 transmission mechanism are also ignored in the numerical simulation; this contributes to  
 277 the larger damping as seen in the experimental data.

### 278 3.4.2. Wave force validation

279 The capability of the present numerical model on predicting the wave force on structures  
 280 is investigated in this section. As such experimental data is not available from Ning et al. [6],  
 281 the experiment proposed in Rodriguez and Spinneken [22] was used. In the latter experiment,  
 282 a 2D rectangular box with a draft of  $b$  and a width of  $2b$  was fixed approximately in the  
 283 centre of a wave flume. The water depth was fixed at  $h = 5b$ . Regular waves were generated  
 284 to interact with the box and the vertical excitation wave forces on the box were measured.  
 285 Two test cases were selected for the current validation: (a)  $kb = 0.4$  and (b)  $kb = 0.7$ ,  
 286 where  $k$  is the wave number. In both cases, the wave steepness  $kA_I$  ( $A_I$  is the incident  
 287 wave amplitude) was 0.10. For full details of the experimental setup, the reader is refer to  
 288 Rodriguez and Spinneken [22].

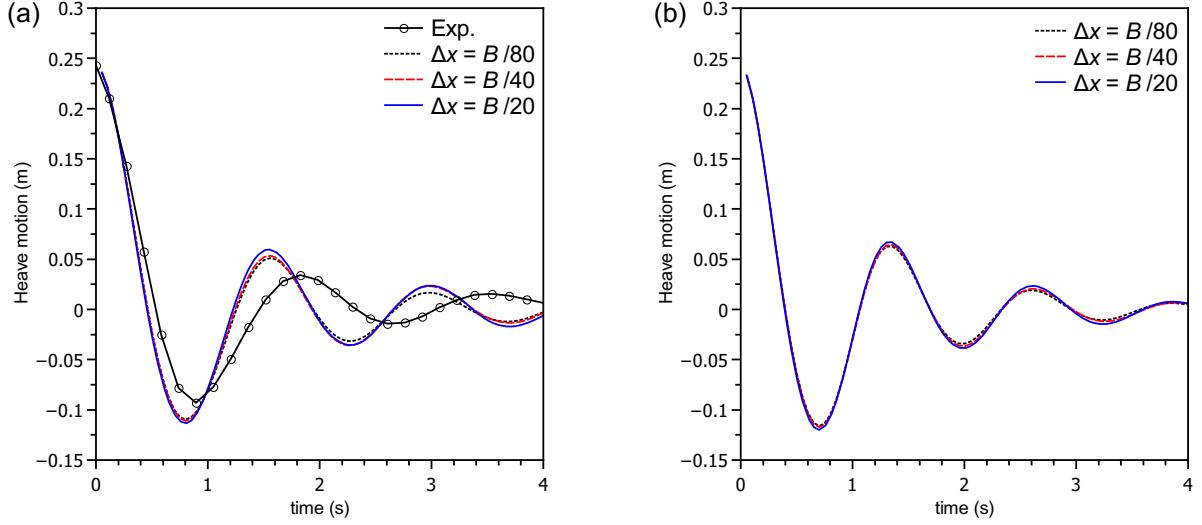


Fig. 7: Grid convergence study on the free decay test of the heave motion of the floating breakwater for (a) rectangular box and (b) box with curve corners (Model 2, see Fig. 6).

289 Fig. 8 presents the comparison of the non-dimensionalised vertical wave force  $F(t)/\rho g A_I b$   
 290 (per unit length in the transverse direction) between the present numerical results and  
 291 the experimental data. From the asymmetric vertical wave force it is shown that strong  
 292 nonlinearities are involved in both test cases, particularly for  $kb = 0.7$ . In general, the  
 293 agreement between the numerical and experimental results is satisfying, which demonstrates  
 294 the capability of the present numerical model in terms of wave force prediction.

### 295 3.4.3. Validation of the WEC-type floating breakwater simulation

296 This section concerns the validation of the present numerical model on modelling the  
 297 hydrodynamic performance of the integrated WEC-type floating breakwater proposed in  
 298 Ning et al. [6]. These correspond to the test cases 1-3 listed in Table 1.

299 Test case 1 concerns the effect of incident wave frequency and no PTO damping force  
 300 was applied. Fig. 9 shows the comparison between numerical and experimental results for  
 301 the non-dimensionalised heave motion response of the floating breakwater,  $\xi/H_i$ , for various  
 302 incident wave periods. In general, it is seen that the numerical results match well with the  
 303 experimental data. Nevertheless, it may be also seen that the overall numerical curve shifts  
 304 slightly to higher relative wave frequencies (i.e.  $B/L$ ) than the experimental curve. This  
 305 is likely due to the fact that the shaft in the PTO system (see Fig. 4) is not simulated in  
 306 the numerical model. As discussed in Section 3.4.1, the shaft in theory increases the overall  
 307 mass of the integrated system and hence lowers its natural frequency.

308 Test case 2 considers two incident wave periods  $T = 1.37$  s and  $1.58$  s (i.e.  $B/L =$

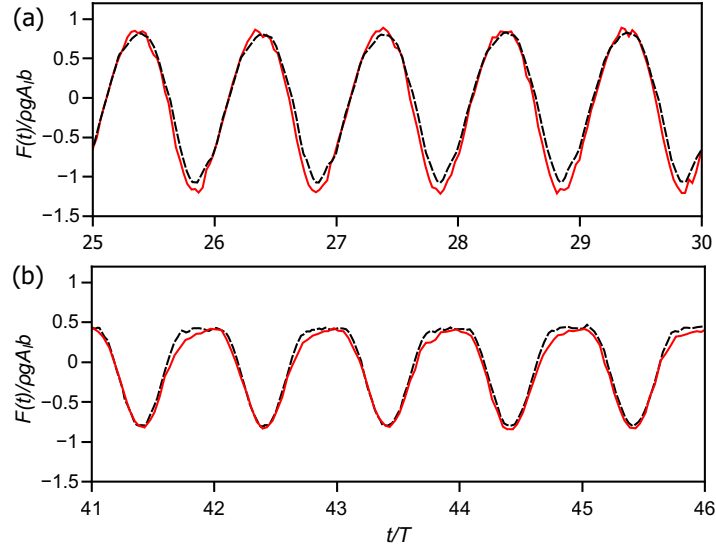


Fig. 8: Comparison of the time-history of the vertical excitation force due to regular waves with  $kA_I = 0.10$ , and (a)  $kb = 0.4$  and (b)  $kb = 0.7$ . Solid line: present numerical result; dashed line: experimental data digitised from Rodriguez and Spinneken [22].

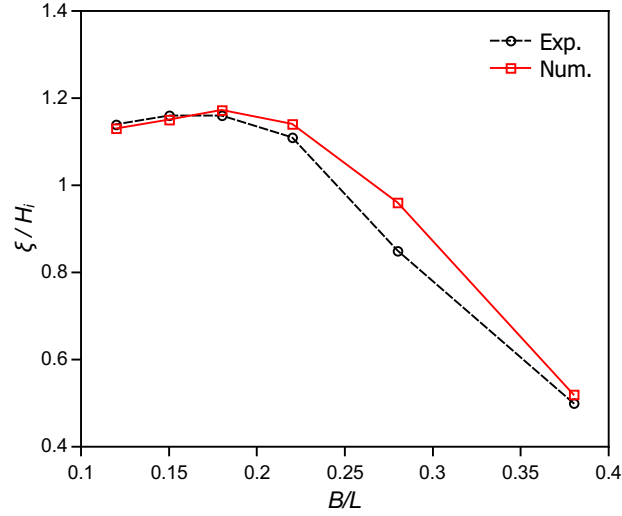


Fig. 9: Comparison of the heave motion response of the floating breakwater for various incident wave periods.

309 0.28 and 0.22) and in both scenarios the PTO damping force was applied, whose magnitude  
 310 was determined by the excitation current (see Table 2). Fig. 10 plots the comparisons for  
 311 the non-dimensional heave response of the floating breakwater  $\xi/H_i$ , the CWR coefficient  
 312  $\eta$  and the transmission coefficient  $K_t$  all as a function of the excitation current. From  
 313 Fig. 10(a) it is seen that for both wave periods the magnitude of the heave response of the  
 314 floating breakwater decreases as the PTO damping force increases. The numerical results



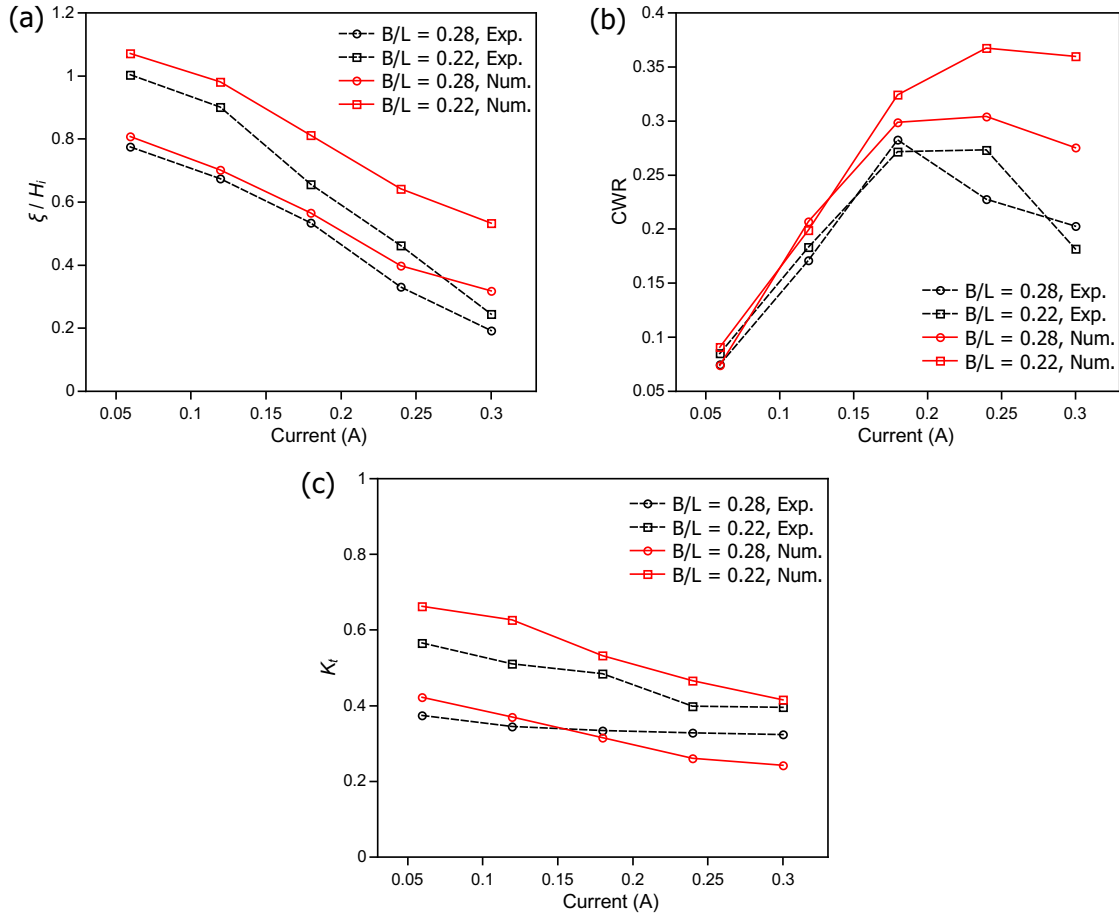


Fig. 10: Comparisons between numerical and experimental results for (a) non-dimensional heave response  $\xi/H_i$ , (b) CWR  $\eta$  and (c) transmission coefficient  $K_t$ .

315 are in general greater than the experimental data, which can be explained by the additional  
 316 friction forces caused in the experiment as well as the above-mentioned effect of neglecting  
 317 the motion of the shaft in the numerical model. Moving to Fig. 10(b), it is seen that  
 318 generally the numerical predictions of the CWR coefficients are greater than the experiment  
 319 due to the larger heave motion responses. However, the numerical model well predicts the  
 320 ranges where optimal peaks of the CWR coefficient occur. Fig. 10(c) shows the comparison  
 321 for the transmission coefficient; it is seen that wave transmission decreases as the heave  
 322 motion of the breakwater decreases (see Fig. 10(a)) and the longer wave period leads to  
 323 larger wave transmission as expected [23]. It is interesting to see that the optimal peak  
 324 of the CWR coefficient occurs in the range where the wave transmission coefficient is low,  
 325 which demonstrates the feasibility of such integrated system with regard to both wave energy  
 326 absorption and wave attenuation.

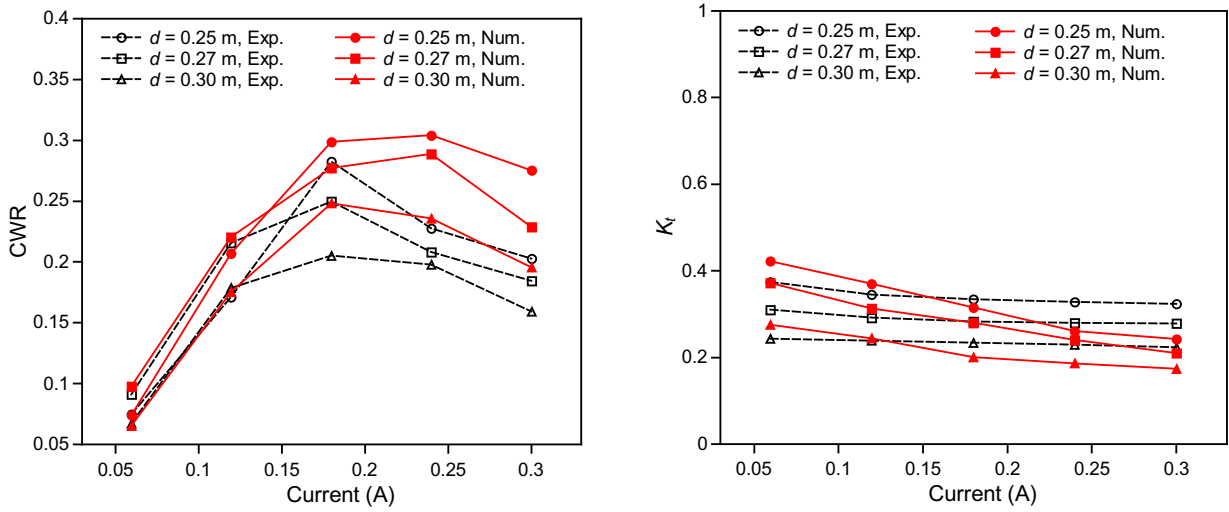


Fig. 11: Comparisons between numerical results and experimental measurements for the CWR coefficient  $\eta$  (left panel) and wave transmission coefficient  $K_t$  (right panel). The results are for  $T = 1.37$  s.

327 In test case 3, the effect of the draft of the floating breakwater is investigated. Fig. 11  
 328 presents the comparisons for the CWR coefficient and the wave transmission coefficient. It  
 329 can be seen that in general the numerical results match reasonably well with the experimental  
 330 data for both the CWR and wave transmission coefficients. The larger draft  $d$  leads to  
 331 smaller magnitude of the heave response of the floating breakwater as it becomes heavier and  
 332 hence smaller CWR coefficients. The larger draft  $d$  also leads to smaller wave transmission  
 333 coefficient. These results are consistent with the findings by Isaacson et al. [23].

334 In short summary, the above comparisons demonstrate that the present PIC model is  
 335 capable of well predicting the key physical processes occurring in these validation test cases.  
 336 Based on that, the optimisation study were conducted and the results are discussed in the  
 337 following sections.

### 338 3.5. Optimisation study

339 The optimisation study in this section aims to further understand the performance of the  
 340 integrated system in the above experiment via changing the shape of the floating breakwater,  
 341 and to provide guidance for designation of a better floating breakwater to achieve high CWR  
 342 but low wave transmission at the same time.

#### 343 3.5.1. Symmetric structure with curve corners

344 Test cases 4 and 5 consider the symmetric models 1-3 with curve corners (see Fig. 6) as  
 345 alternative floating breakwaters and all the other settings, such as the PTO damping force,

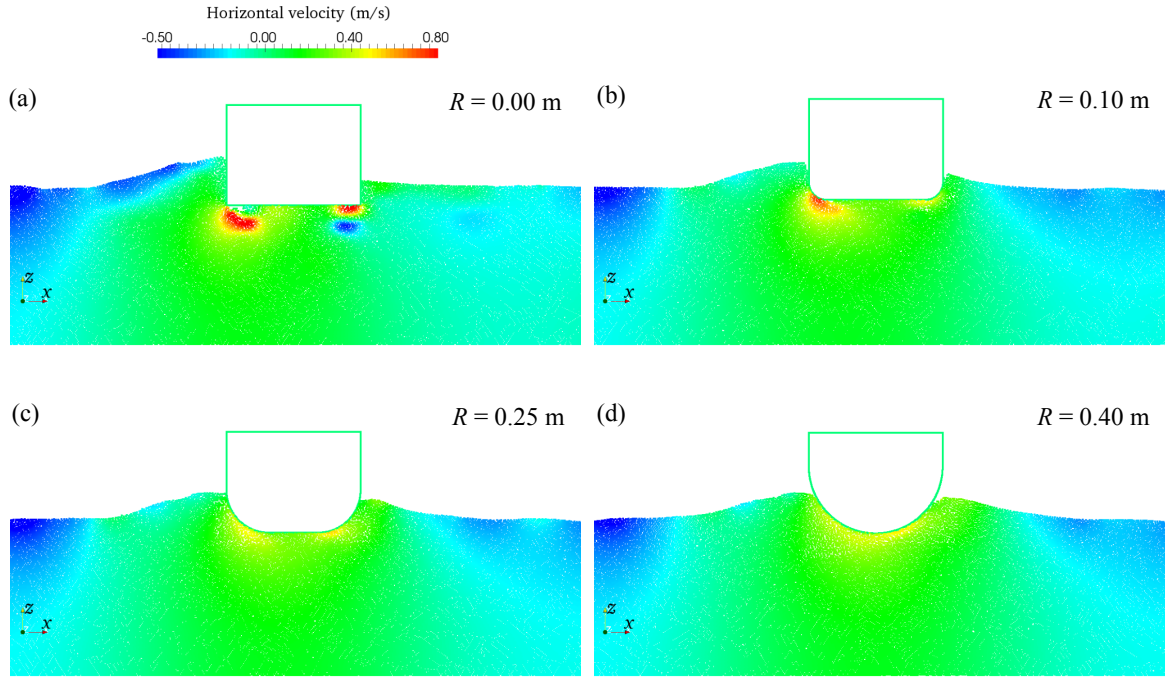


Fig. 12: Snapshot of the numerical results for different floating breakwaters at similar time instants. The test conditions are  $T = 1.58$  s,  $I = 0.06$  A and  $d = 0.25$  m.

346 are set the same as those used in test cases 2 and 3, respectively.

347 [Fig. 12](#) shows the snapshot of the numerical results run by using different floating break-  
 348 waters. It is seen that by changing the straight corners to curve corners, the velocity gradient  
 349 of the fluid field around the corners becomes smaller as the radii of the corners increase.  
 350 Also, it seems that the wave can move past the breakwater more easily when the radii of  
 351 the corners increase.

352 For test case 4, [Fig. 13](#) presents the numerical results of the CWR coefficient and the  
 353 wave transmission coefficient for various symmetric floating breakwaters (models 1-3, see  
 354 [Fig. 6](#)). From the CWR coefficient plots, it is seen that the floating breakwaters with curve  
 355 corners ( $R > 0.0$  m) generally perform better than the rectangular box ( $R = 0.0$  m), in  
 356 terms of wave energy extraction. This is likely due to that much less vortices were generated  
 357 around the corners when curve corners were used (see [Fig. 12](#)) and hence a much smaller  
 358 eddy making damping was induced. In particular, for the case when  $T = 1.37$  s ( $B/L =$   
 359  $0.28$ ), the optimal CWR coefficient is increased by approximately 40%. This significant  
 360 increase may be also due to that  $T = 1.37$  s is close to the natural periods of the floating  
 361 breakwaters with curve corners, which range from approximately 1.43 s to 1.18 s as the radii

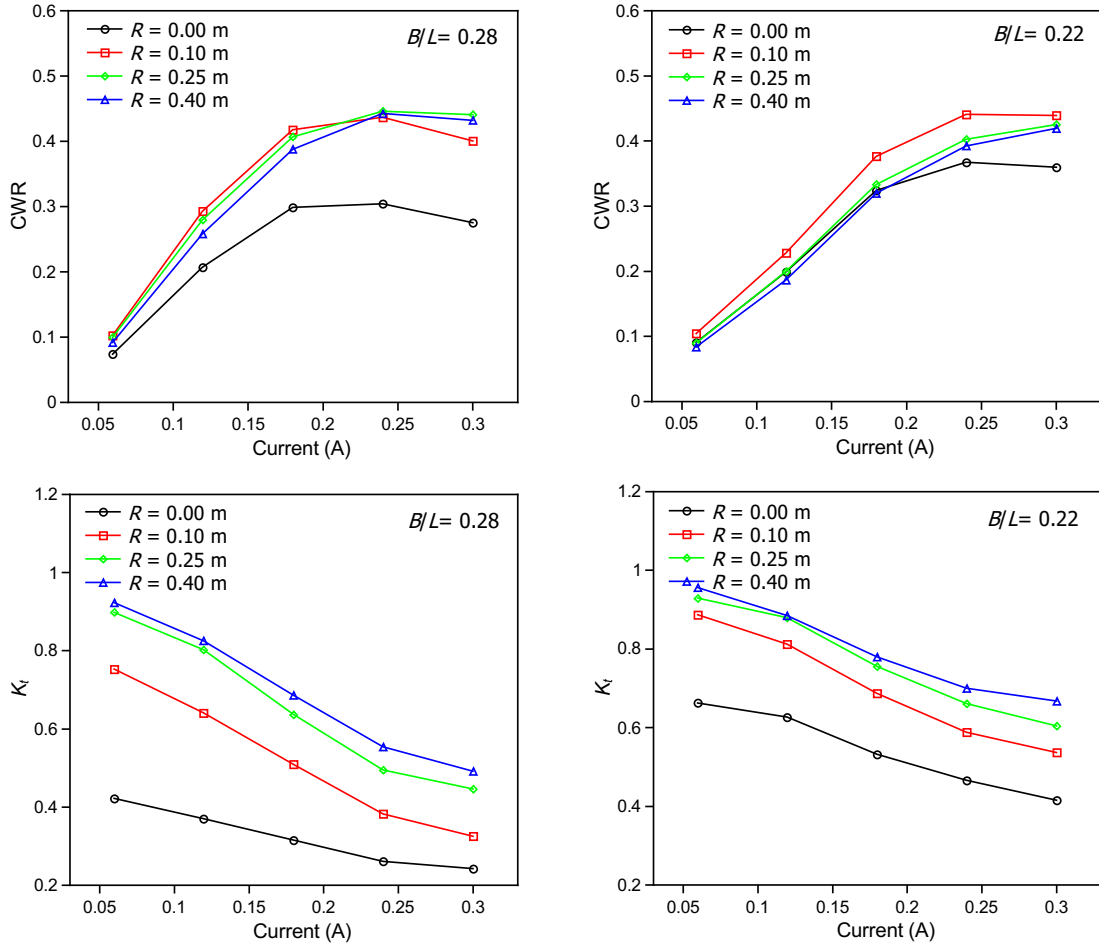


Fig. 13: Numerical results of the CWR coefficient (upper panels) and wave transmission coefficient  $K_t$  (lower panels) for symmetric floating breakwaters with various radii of the corners. The draft  $d = 0.25$  m for all cases.

362 of the corners increase from 0.10 m to 0.40 m according to a number of free decay tests in the  
 363 numerical model. On the other hand, from the results of the wave transmission coefficient,  
 364 it is seen straightforwardly that as the radii of the structure corners increase, the wave  
 365 transmission coefficient increases as well. The original rectangular box achieves the best  
 366 performance from this point of view. Nevertheless, it is observed that the breakwater with  
 367 the smallest curve corners, i.e. model 1 ( $R = 0.10$  m), also leads to small wave transmission  
 368 coefficients that are close to those of the rectangular box, particularly in the ranges where the  
 369 optimal CWR occurs. Therefore, considering the outstanding performance on wave energy  
 370 extraction, model 1 with small curve corners may prove to be an optimised design for the  
 371 floating breakwater in such integrated system.

372 Test case 5 considers the effect of the draft on the performance of the integrated system

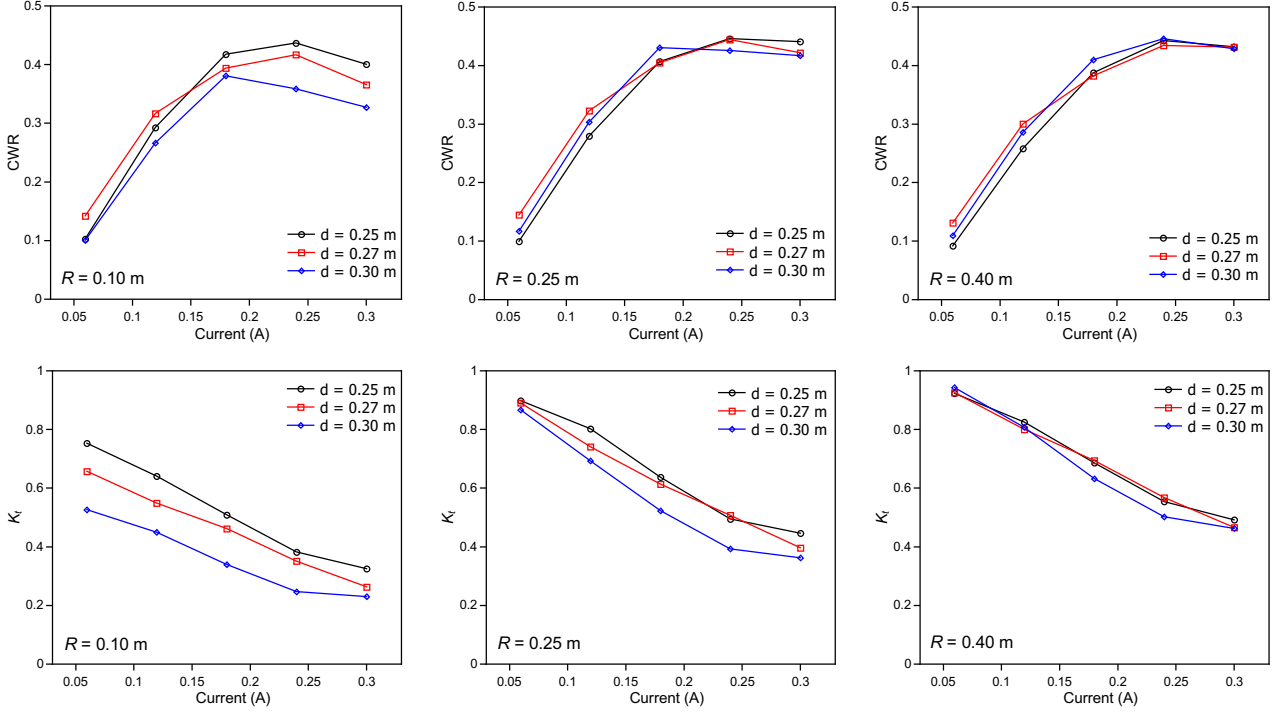


Fig. 14: Numerical results of the CWR coefficient (upper panels) and wave transmission coefficient  $K_t$  (lower panels) for symmetric floating breakwaters subjected to three different drafts. The wave period is 1.37 s.

373 when models 1-3 (see Fig. 6) are used as the floating breakwater. Fig. 14 plots the numerical  
 374 results for both the CWR and wave transmission coefficients for models 1-3 all subjected  
 375 to three different drafts. It can be seen from Fig. 14 that the influence of the draft on  
 376 the performance of the integrated system reduces as the radii of the curve corners increase.  
 377 While the small curve breakwater case ( $R = 0.10$  m) shows a similar effect of the draft to  
 378 that in the rectangular box case (see Fig. 11), the full curve breakwater case ( $R = 0.40$  m)  
 379 illustrates that the draft has a very weak effect on the performance of the integrated system.  
 380 This more or less demonstrates that the floating breakwater with small curve corners has  
 381 more flexibilities than those with large curve corners.

### 382 3.5.2. Asymmetric structure with curve and straight corners

383 The test cases presented above show that the performance of the integrated WEC-type  
 384 floating breakwater can be optimised by modifying the straight corners of the floating break-  
 385 water to small curve corners. It may be also concluded that the curve corners result in large  
 386 CWR due to a reduction of the eddy making damping but also large wave transmission as  
 387 waves can move past the curve corners more easily, while the straight corners do the oppo-  
 388 site. So, it may be interesting to see the results of a floating breakwater with both a curve

389 and a straight corner. Test case 6 investigates the performance of the asymmetric models 4  
390 and 5 (see Fig. 6), which have only one small curve corner ( $R = 0.10$  m) in the seaward side  
391 and in the leeward side, respectively. The other test conditions are set the same as those  
392 used in test case 2.

393 Fig. 15 presents the results of the CWR and wave transmission coefficients for the asym-  
394 metric models 4 and 5, in comparison with those of the rectangular box and the symmetric  
395 model 1 ( $R = 0.10$  m). It can be seen that in general model 4 achieves a similar performance  
396 to model 1 in terms of the CWR coefficient, but with the wave transmission coefficient being  
397 further reduced. On the other hand, model 5 produces CWR coefficients close to those by  
398 the rectangular box, but with larger wave transmission coefficients. The reason behind this  
399 is likely to be that the wave height in the seaward side is larger than that in the leeward  
400 side and hence the eddy making damping around the seaward side corner of the rectangular  
401 box is predominant; by modifying the seaward side straight corner to a small curve corner,  
402 the major eddy making damping is significantly reduced and hence larger CWR coefficients  
403 were achieved. Furthermore, keeping the leeward side straight corner can more or less help  
404 reduce wave transmission as discussed above. These lead to the conclusion that model 4 is  
405 a further optimisation of the small curve model 1, while model 5 is not recommended.

#### 406 4. Conclusions

407 This paper presents a numerical study of the hydrodynamic performance of a vertical  
408 pile-restrained WEC-type floating breakwater, which is experimentally investigated in Ning  
409 et al. [6]. The numerical model solves the incompressible Navier-Stokes equations for free-  
410 surface flows using the PIC method, and incorporates a Cartesian cut cell based two-way  
411 strong coupling algorithm for fluid-structure interaction. The numerical model is first val-  
412 idated against the experimental measurements and then used for an optimisation study.  
413 The validation results show that the PIC model can well capture the key physical processes  
414 occurring in this complex wave-structure interaction scenario. Regarding the optimisation  
415 study, the results show that by modifying only the seaward side straight corner of the rect-  
416 angular box floating breakwater proposed in Ning et al. [6] to a small curve corner, the  
417 integrated system achieves significantly more wave energy extraction at the cost of only a  
418 slight increase in wave transmission. For further research, a new physical experiment based  
419 on the optimised shape of the floating breakwater is under consideration.

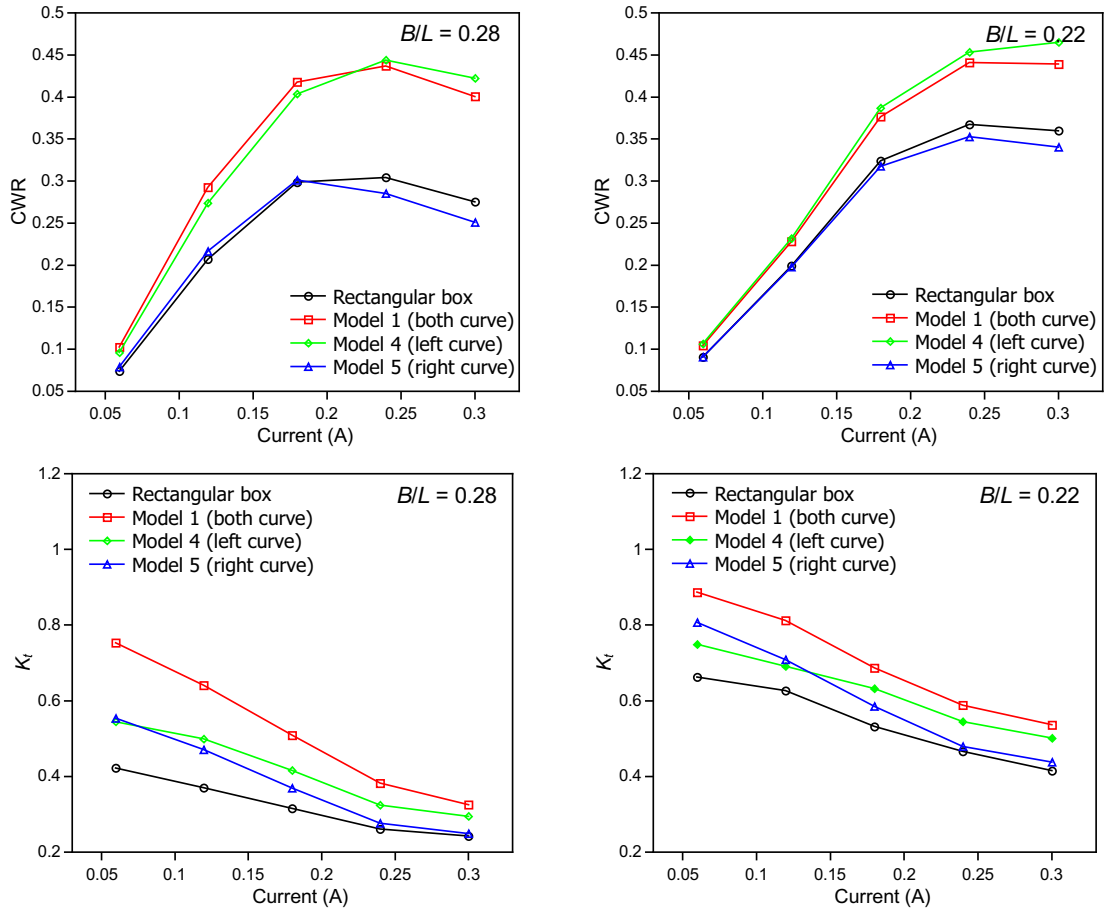


Fig. 15: Numerical results of the CWR coefficient (upper panels) and wave transmission coefficient  $K_t$  (lower panels) for asymmetric base models 4 and 5, in comparison with those by the rectangular box and model 1.

## 420 Acknowledgements

421 This work is supported by the UK Engineering and Physical Sciences Research Council  
 422 (EPSRC) (Grant No. EP/R007519/1), the Open Funding of the State Key Laboratory of  
 423 Coastal and Offshore Engineering at Dalian University of Technology (Grant No. LP1803)  
 424 and the Royal Academy of Engineering (RAE) (Grant No. UK-CIAPP/73).

## 425 References

- 426 [1] J. Dai, C. M. Wang, T. Utsunomiya, W. Duan, Review of recent research and developments on floating  
 427 breakwaters, *Ocean Engineering* 158 (2018) 132 – 151.  
 428 [2] A. G. L. Borthwick, Marine renewable energy seascape, *Engineering* 2 (2016) 69 – 78.  
 429 [3] M. A. Mustapa, O. B. Yaakob, Y. M. Ahmed, C.-K. Rheem, K. K. Koh, F. A. Adnan, Wave energy

- 430 device and breakwater integration: A review, *Renewable and Sustainable Energy Reviews* 77 (2017)  
431 43 – 58.
- 432 [4] C. Michailides, D. C. Angelides, Modeling of energy extraction and behavior of a Flexible Floating  
433 Breakwater, *Applied Ocean Research* 35 (2012) 77 – 94.
- 434 [5] F. He, Z. Huang, A. W.-K. Law, An experimental study of a floating breakwater with asymmetric  
435 pneumatic chambers for wave energy extraction, *Applied Energy* 106 (2013) 222 – 231.
- 436 [6] D. Ning, X. Zhao, M. Gteman, H. Kang, Hydrodynamic performance of a pile-restrained WEC-type  
437 floating breakwater: An experimental study, *Renewable Energy* 95 (2016) 531 – 541.
- 438 [7] F. H. Harlow, A Machine Calculation Method for Hydrodynamic Problems, Technical Report LAMS-  
439 1956, Los Alamos Scientific Laboratory, Los Alamos, 1955.
- 440 [8] F. H. Harlow, The Particle-In-Cell computing method for fluid dynamics, in: B. Alder (Ed.), *Methods*  
441 *in Computational Physics*, Academic Press, New York, 1964, pp. 319–343.
- 442 [9] F. H. Harlow, Fluid dynamics in Group T-3 Los Alamos National Laboratory: (LA-UR-03-3852),  
443 *Journal of Computational Physics* 195 (2004) 414 – 433.
- 444 [10] J. U. Brackbill, H. M. Ruppel, FLIP: A method for adaptively zoned, Particle-In-Cell calculations of  
445 fluid flows in two dimensions, *J. Comp. Phys.* 65 (1986) 314–343.
- 446 [11] J. U. Brackbill, D. B. Kothe, H. M. Ruppel, FLIP: A low-dissipation, Particle-In-Cell method for fluid  
447 flow, *Computer Physics Communications* 48 (1988) 25–38.
- 448 [12] E. Edwards, R. Bridson, A high-order accurate Particle-In-Cell method, *International Journal for*  
449 *Numerical Methods in Engineering* 90 (2012) 1073–1088.
- 450 [13] J. M. Maljaars, R. J. Labeur, M. Möller, A hybridized discontinuous galerkin framework for high-order  
451 particlemesh operator splitting of the incompressible navierstokes equations, *Journal of Computational*  
452 *Physics* 358 (2018) 150 – 172.
- 453 [14] W. Wang, D. M. Kelly, A high-order PIC method for advection-dominated flow with application to  
454 shallow water waves, *International Journal for Numerical Methods in Fluids* 87 (2018) 583–600.
- 455 [15] D. M. Kelly, Full particle PIC modelling of the surf and swash zones, in: *Proc. 33rd Int. Conf. Coast.*  
456 *Eng., A.S.C.E., Santander, 2012*, pp. 77–92.
- 457 [16] D. M. Kelly, Q. Chen, J. Zang, PICIN: A Particle-In-Cell solver for incompressible free surface flows  
458 with two-way fluid-solid coupling, *SIAM Journal on Scientific Computing* 37 (2015) B403–B424.
- 459 [17] Q. Chen, J. Zang, A. S. Dimakopoulos, D. M. Kelly, C. J. Williams, A Cartesian cut cell based two-way  
460 strong fluid-solid coupling algorithm for 2D floating bodies, *Journal of Fluids and Structures* 62 (2016)  
461 252 – 271.
- 462 [18] Q. Chen, J. Zang, D. M. Kelly, A. S. Dimakopoulos, A 3D parallel particle-in-cell solver for wave  
463 interaction with vertical cylinders, *Ocean Engineering* 147 (2018) 165 – 180.
- 464 [19] Q. Chen, Development of A Full Particle PIC Method for Simulating Nonlinear Wave-Structure Inter-  
465 action, Ph.D. thesis, University of Bath, 2017.
- 466 [20] A. J. Chorin, Numerical solution of the Navier–Stokes equations, *Math. Comput.* 22 (1968) 745–762.
- 467 [21] Q. Chen, D. M. Kelly, A. S. Dimakopoulos, J. Zang, Validation of the PICIN solver for 2D coastal  
468 flows, *Coastal Engineering* 112 (2016) 87 – 98.
- 469 [22] M. Rodriguez, J. Spinneken, A laboratory study on the loading and motion of a heaving box, *Journal*  
470 *of Fluids and Structures* 64 (2016) 107 – 126.



471 [23] M. Isaacson, J. Baldwin, S. Bhat, Wave propagation past a pile-restrained floating breakwater, Inter-  
472 national Journal of Offshore and Polar Engineering 8 (1998) 265–269.